A High-Efficiency Sulfur/Carbon Composite Based on 3D Graphene Nanosheet@Carbon Nanotube Matrix as Cathode for Lithium–Sulfur Battery

Ze Zhang, Ling-Long Kong, Sheng Liu, Guo-Ran Li, and Xue-Ping Gao**

Carbon materials have attracted extensive attention as the host materials of sulfur for lithium–sulfur battery, especially those with 3D architectural structure. Here, a novel 3D graphene nanosheet–carbon nanotube (GN–CNT) matrix is obtained through a simple one-pot pyrolysis process. The length and density of CNTs can be readily tuned by altering the additive amount of carbon source (urea). Specifically, CNTs are in situ introduced onto the surface of the graphene nanosheets (GN) and show a stable covalent interaction with GN. Besides, in the GN–CNT matrix, cobalt nanoparticles with different diameters exist as being wrapped in the top of CNTs or scattering on the GN surface, and abundant heteroatoms (N, O) are detected, both of which can help in immobilizing sulfur species. Such a rationally designed 3D GN–CNT matrix makes much more sense in enhancing the electrochemical performance of the sulfur cathode for rapid charge transfer and favorable electrolyte infiltration. Moreover, the presence of dispersed cobalt nanoparticles is beneficial for trapping lithium polysulfides by strong chemical interaction, and facilitating the mutual transformation between the high-order polysulfides and low-order ones. As a result, the S/GN–CNT composite presents a high sulfur utilization and large capacity on the basis of the S/GN–CNT composite as active material.

1. Introduction

Elemental sulfur, as a promising candidate for cathodes, offers a high theoretical specific capacity of 1675 mA h g^{-1}, and also is naturally abundant, low-cost, and produced in quantity.[1] Since with the metallic Li as the anode, the lithium–sulfur (Li–S) battery enables an ultrahigh gravimetric energy density of 2600 W h kg^{-1}.[2] However, the development of Li–S battery is plagued by several challenges that must be addressed. First of all, sulfur is both electrically and ionically insulating, as well as its lithiated product Li_2S, which necessitates the incorporation of sulfur into a conductive matrix.[3] In addition, quite different from traditional Li intercalation compounds, sulfur suffers electrochemical dissolution and deposition reactions and generates a series of polysulfide (PS_n) species, of which high-order PS_n ($4 \le n \le 8$) are soluble in ether-based electrolyte and prone to diffuse to the anode side for reducing deeply to the insoluble Li_2S_2 and Li_2S. Correspondingly, Li_2S_2 and Li_2S could migrate back to the cathode and be oxidized.[4] The so-called "shuttle effect" leads to an irreversible loss of active sulfur and a fast degradation of cycle stability. Consequently, during the redox reaction, the repetitive dissolution and deposition reactions of the PS_n passivate both cathode and anode gradually, resulting in a considerable increase of the electrode impedance.[5] Moreover, the density difference between sulfur (2.07 g cm^{-3}) and Li_2S (1.66 g cm^{-3}) leads to a significant volume expansion, which is adverse to the mechanical strength of sulfur cathode.[2c,6] All of these factors restrict severely the electrochemical performance of sulfur cathode.

To date, upsurge of attention has been paid in fabricating high-efficiency and stable sulfur cathode, the vital component of the Li–S battery. These efforts focus on developing novel nanocomposites by incorporating sulfur into various host materials, such as carbonaceous materials (including porous carbon,[7] hollow carbon spheres,[8] carbon nanotube/fibers,[9] graphene and its derivatives,[10] or hybrid carbon hosts,[11]) conducting polymers,[12] metal oxides,[13] and metal or covalent organic frameworks.[14] These host materials are expected to promote the electron transfer, accommodate the volumetric expansion, and trap the soluble PS_n. In this respect, carbonaceous materials are proven to be a promising option owing to their excellent electrical conductivity, outstanding mechanical strength, and multiple architectures. Typically, the members with higher-dimensional contrast structure are endowed with exclusive superiority in compositing with sulfur. In detail, carbon nanotubes (CNTs) possess classic 1D structure and exhibit a self-weaving

Z. Zhang, L.-L. Kong, Dr. S. Liu, Prof. G.-R. Li, Prof. X.-P. Gao
Institute of New Energy Material Chemistry
School of Materials Science and Engineering
National Institute for Advanced Materials
Nankai University
Tianjin 300350, China
E-mail: guoranli@nankai.edu.cn; xpgao@nankai.edu.cn
Prof. X.-P. Gao
Collaborative Innovation Center of Chemical Science and Engineering (Tianjin)
Tianjin Key Laboratory of Metal and Molecule Based Material Chemistry
Nankai University
Tianjin 300350, China

DOI: 10.1002/aenm.201602543

behavior to construct an interwoven conductive network for fast transfer of electrons.[8d,9a] Meanwhile, the graphene nanosheet (GN), a typical 2D material, can be easily modified with oxygen-containing functional groups and by doping heteroatoms, which makes it an amazing matrix to fabricate sulfur/graphene composite with large capacity. It is known that sulfur can be filled in the abundant pores of micro/mesoporous carbon materials. As for CNTs or graphene and its derivatives, sulfur species precipitate mainly on the outer surface since the sulfur content is expected to be higher than 70 wt%,[6b] resulting in fast diffusion into the electrolyte owing to the direct contact with the electrolyte. In response, the design concept combining 1D CNTs with 2D graphene to form 3D structural GN–CNT matrix becomes well-reasoned. Apart from making full use of the merits of the two components, the resultant open, porous, and 3D conductive network in the designed matrix is also believed to transfer electrons rapidly, store sulfur species, and trap soluble PS_n well. As a result, sulfur cathode based on the GN–CNT matrix shows superior electrochemical performance.[15]

In fact, the key issue is how to obtain an effective combination between CNTs with graphene experimentally to ensure the significant improvement of the electrochemical performance for sulfur cathode. Fortunately, fabricating 3D GN–CNT matrix from self-assembly is adopted with the promotion of electrostatic interaction.[15b] The RGO@MWCNT–W/S composite exhibits an initial discharge capacity of 1164.5 mA h $g^{-1}_{(sulfur)}$, and remains a large capacity of 891.5 mA h $g^{-1}_{(sulfur)}$ after 200 cycles at 1 C, when 68.93 wt% of sulfur is incorporated into the RGO@MWCNT–W matrix. Another strategy is chemical vapor deposition method. Typically, in these matrices, CNTs are covalently anchored on graphene sheets, resulting in an extraordinary conductivity. In this respect, a variety of works on the incorporation of CNTs and graphene are done by Zhang and co-workers.[16] Noticeably, it is the producing covalent C—C bond between CNTs and graphene sheets that makes the matrix very promising in fabricating desirable sulfur cathode.

However, the two methods reported are still limited by the involved uncontrollable and intricate processes. Thus, an innovative, feasible, and controllable strategy should be explored. As to this aspect, Sun and co-workers reported a one-pot pyrolysis method to controllably grow CNTs on GN surface to obtain GN–CNT matrix with 3D interpenetrating structure.[17] When used as an electrode material for supercapacitor, the resultant matrix shows good electrochemical performance. Considering that such a unique nanostructure exactly suits for immobilizing sulfur, in this contribution, 3D GN–CNT matrix is prepared with urea as the carbon source and metallic cobalt reduced from Co^{2+} as the catalyst, and then sulfur is incorporated into the GN–CNT matrix via a chemical deposition method to obtain S/GN–CNT composite. As a comparison, S/GN composite is also prepared. Here, GN is obtained in the same way with that of the GN–CNT matrix, but without the addition of urea and Co^{2+}. As expected, the as-prepared S/GN–CNT composite exhibits excellent utilization of active sulfur, superior cycle stability, and outstanding high rate capability, which obviously exceed that of S/GN composite.

2. Results and Discussion

The GN–CNT matrix is obtained via a simple one-pot pyrolysis process, as reported previously.[17] In the beginning, cobalt nitrate is added into the graphene oxide (GO) solution under stirring to promote the adsorption of Co^{2+} on GO surface through an electrostatic interaction between Co^{2+} and the oxygen-containing functional groups. After that, urea (6.0 g) is added, and the mixture is stirred until complete dissolution of urea. Thus, the hydrophilic urea could form stable coordination compound with Co^{2+}, which is assumed to prevent the restack of GO sheets during the following evaporating and high-temperature processes. Besides, urea serves as a carbon source for the growth of CNTs during the high-temperature decomposition, where urea is pyrolyzed into various CN gases ($C_2N_2^+$, $C_3N_2^+$, and $C_3N_3^+$)[18] and Co^{2+} is reduced to metallic cobalt by those reducing gases. As a result, these CN gases tend to form CNTs in situ on the GN surface at the aid of cobalt catalyst. It should be noticed that these CN gases are believed to loosen GN layers to create pores, resulting in a porous structure with large surface area. Finally, the as-prepared GN–CNT matrix is adopted to combine with sulfur to fabricate S/GN–CNT composite via a reaction of sodium thiosulfate with dilute hydrochloric acid.

In the GN–CNT matrix, the metallic cobalt produced is confirmed by the three typical peaks at 44.2°, 51.6°, and 75.9°, respectively, consistent with (111), (200), and (220) planes of Co (PDF#89-4307), as seen in X-ray diffraction (XRD) patterns in **Figure 1**. It is believed that in the pyrolysis process of urea, Co^{2+} is reduced to metallic cobalt and the latter promotes the in situ growth of CNTs on the GN surface. As to the S/GN–CNT composite, sulfur exists in a crystalline state with typical sharp peaks. On the other hand, since such a growth of CNTs might

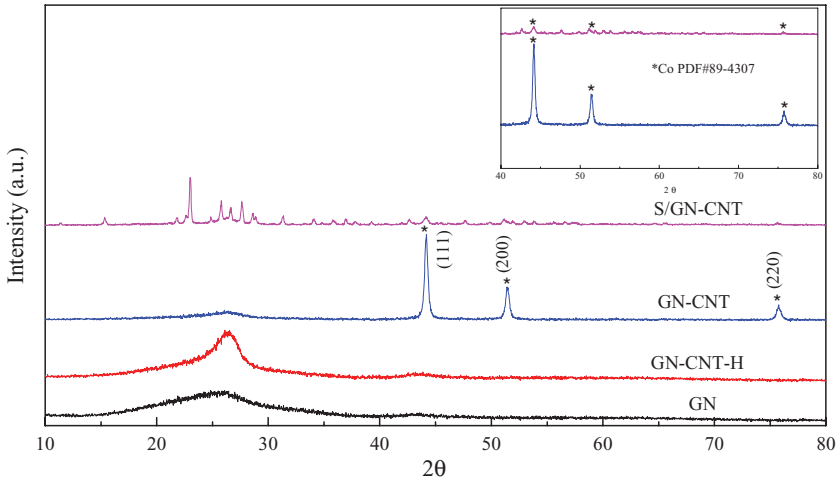

Figure 1. XRD patterns of GN, GN–CNT matrix (after being rinsed by hydrochloric acid, marked as GN–CNT–H) and S/GN–CNT composite. (The inset shows XRD patterns with the 2θ range from 40° to 80°.)

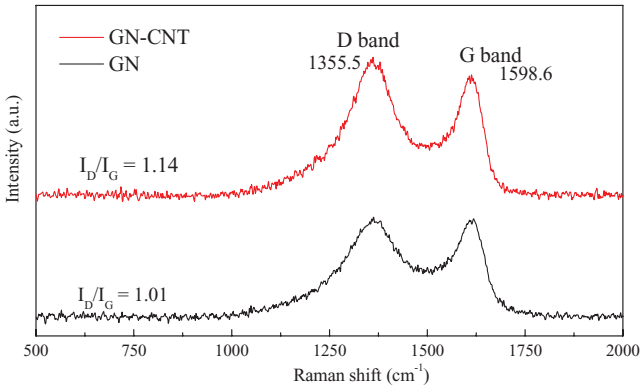

Figure 2. Raman spectra of GN and GN–CNT matrix.

follow the principle of tip growth mechanism,[19] the produced metallic cobalt nanoparticles are likely to be wrapped in the top of CNTs. Some Co nanoparticles survive from the invasion of excess H^+ during its reaction with $S_2O_3^{2-}$ in the preparation process of S/GN–CNT composite since the surface of the GN–CNT matrix is covered by quickly deposited sulfur to prevent the further corrosion of inner Co nanoparticles with acid. Thus, as shown in the XRD pattern, the typical peaks of metallic cobalt still remain but become weaker for the S/GN–CNT composite. Of course, when the GN–CNT sample is rinsed by diluted hydrochloric acid, the diffraction peaks of metallic cobalt disappear almost in the sample (GN–CNT–H) owing to the adequate reaction of metallic cobalt with hydrochloric acid.

Raman spectroscopy is performed to identify the introduction of CNTs onto GN surface, as shown in **Figure 2**. It can be seen that no difference is observed for the peaks of D band and G band, identified at 1355.5 and 1598.6 cm^{-1}, respectively. However, the intensity ratio (I_D/I_G) of D band and G band of GN is ≈1.01, inferior to that (I_D/I_G = 1.14) of GN–CNT matrix, indicating that the GN–CNT matrix possesses a more disordered structure owing to the introduction of CNTs. In addition, now that various CN gases are produced to form CNTs, the introduction of CNTs onto GN not only modifies its structure and morphology, but also increases the specific surface area (SSA). Thus, the Brunauer–Emmett–Teller surface area analyzer is used to measure the SSA (Figure S1, Supporting Information). It comes as no surprise that the SSA of GN–CNT matrix is measured as 917.8 m^2 g^{-1}, which is nearly threefold greater than that of GN (334.8 m^2 g^{-1}). Such an enhancement in SSA can be ascribed to the generation of abundant pores by the release of CN gases and the effective intercalation and distribution of CNTs between graphene layers. In addition, thermogravimetric analysis (TGA) profiles are provided in Figure S2 (Supporting Information) to confirm the sulfur content. As seen, all of the composites possess high sulfur content based on the TGA profiles.

Scanning electron microscopy (SEM) images of the obtained GN–CNT matrix and S/GN–CNT composite are given in **Figure 3**. The GN–CNT matrix has a loose and porous presentation with well-defined CNTs adhering on the surface of GN, where CNTs show a diameter range of 20–75 nm and a length range of 120–400 nm (Figure 3a). In particular, CNTs are grown on both sides of GN as shown from the side view of the matrix (Figure 3b). It should be noticeable that the loose and porous structure, created by the abundant CN gases during the pyrolysis process of urea, is beneficial for immobilizing sulfur

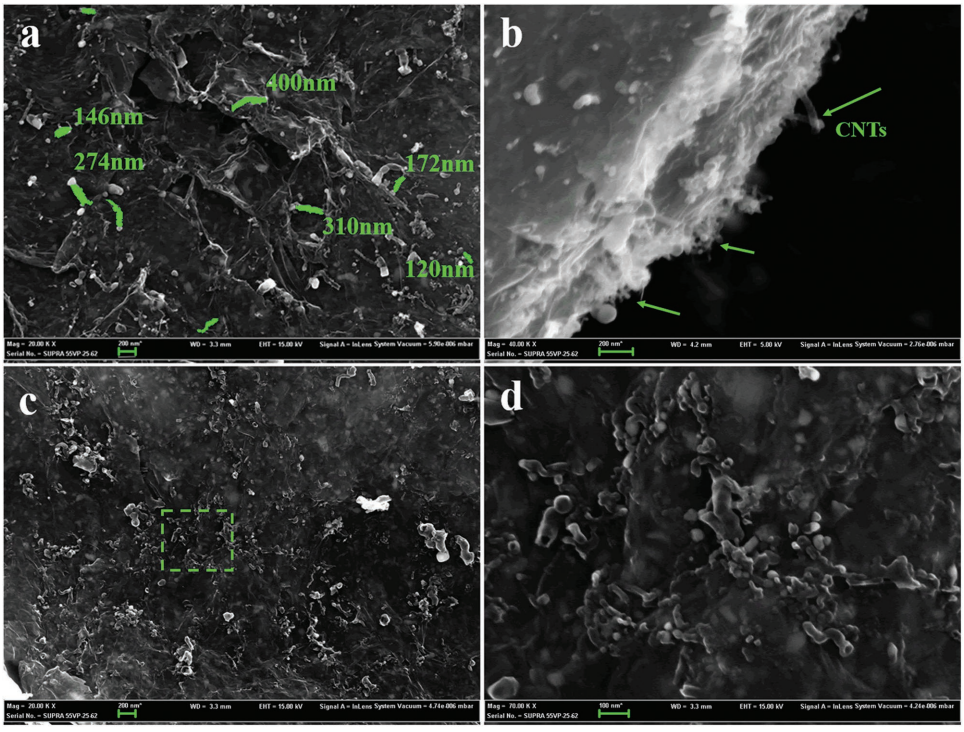

Figure 3. SEM images of a,b) GN–CNT matrix and c,d) S/GN–CNT composite.

species. The as-prepared S/GN–CNT composite presents more smooth and dense morphology, where the diameter of CNTs becomes larger owing to the deposition of massive sulfur on the outer surface of the matrix. Apart from succeeding in growing CNTs on the GN surface, the length and density of CNTs are readily tuned by altering the amount of additive urea in the process. Here, both the length and density of CNTs are increased with increasing the amount of additive urea, as shown in Figure S3 (Supporting Information). The structure of the resultant matrix is easily controllable, and the performance of the corresponding sulfur/carbon (S/C) composite can be optimized consequently. In addition, the chemical composition of the as-prepared GN-CNT is measured by energy dispersive spectometer (EDS) (Figure S4, Supporting Information). The Co content is measured to be 36.51 wt% in the GN–CNT matrix. Meanwhile, the doped N and O atoms can also be detected. Here, the coexistent Co and heteroatoms in the GN–CNT matrix are beneficial for entrapping sulfur species.[14d]

Furthermore, to identify the interaction between CNTs and GN, the GN–CNT matrix is powerfully ultrasonicated for half an hour in absolute ethanol. As shown in **Figure 4**a, CNTs still adhere well to GN after ultrasonic treatment, implying a stable covalent linkage with GN, rather than being physically adsorbed on the GN surface. Besides, the cobalt catalysts appear as nanoparticles with a diameter ranging from 20 to 75 nm, wrapped in the top of CNTs or distributed randomly on the GN surface. It is noticeable that the diameter of cobalt nanoparticles matches well with that of the resultant CNTs, which makes it clear that the formation of CNTs follows the top growth mechanism. Typically, the produced CNT has an external diameter of 38 nm and inner diameter of 32 nm as seen in Figure 4b. Here, CNTs exist as multiwalled with the wall thickness of 6 nm (Figure 4c). As to the S/GN–CNT composite (Figure 4d), the structure incorporating CNTs with GN is clearly seen even after the deposition of massive sulfur, and various cobalt nanoparticles as black dots are dispersed in the composite. The scanning-transmission electron microscopy (STEM) image and EDS maps of selected region are shown in Figure 4e–k. Those black dots are identified as metallic cobalt according to mass-thickness contrast, which is consistent with XRD analysis, and sulfur is uniformly distributed. Moreover, it is indicated from the abundant distribution of element N and O that the pyrolysis of urea can effectively lead to the nitridation and oxidation of C atoms, which is beneficial for trapping and confining polysulfides. In particular, the distribution of sulfur is highly matched with that of Co in the S/GN–CNT composite (Figure 4h–j), implying the strong chemical interaction between sulfur and cobalt.

Deep understanding of the chemical composition in the GN–CNT matrix and corresponding S/GN–CNT composite is revealed by X-ray photoelectron spectra (XPS; **Figure 5**). In the case of the GN–CNT matrix, the fitted C 1s core level (Figure 5a) shows three peaks at 284.7, 285.5, and 286.8 eV, which can be identified as C=C, C=N, and C–N species, respectively. Besides, the N 1s core level can be fitted into three typical peaks at the binding energy of 398.6, 400.0, and 401.3 eV, consistent with pyridinic, pyrrolic, and graphitic nitrogen, respectively, as seen in Figure 5b. Therefore, the formation of C–N bonds can be confirmed in the pyrolysis process of urea. Owing to the

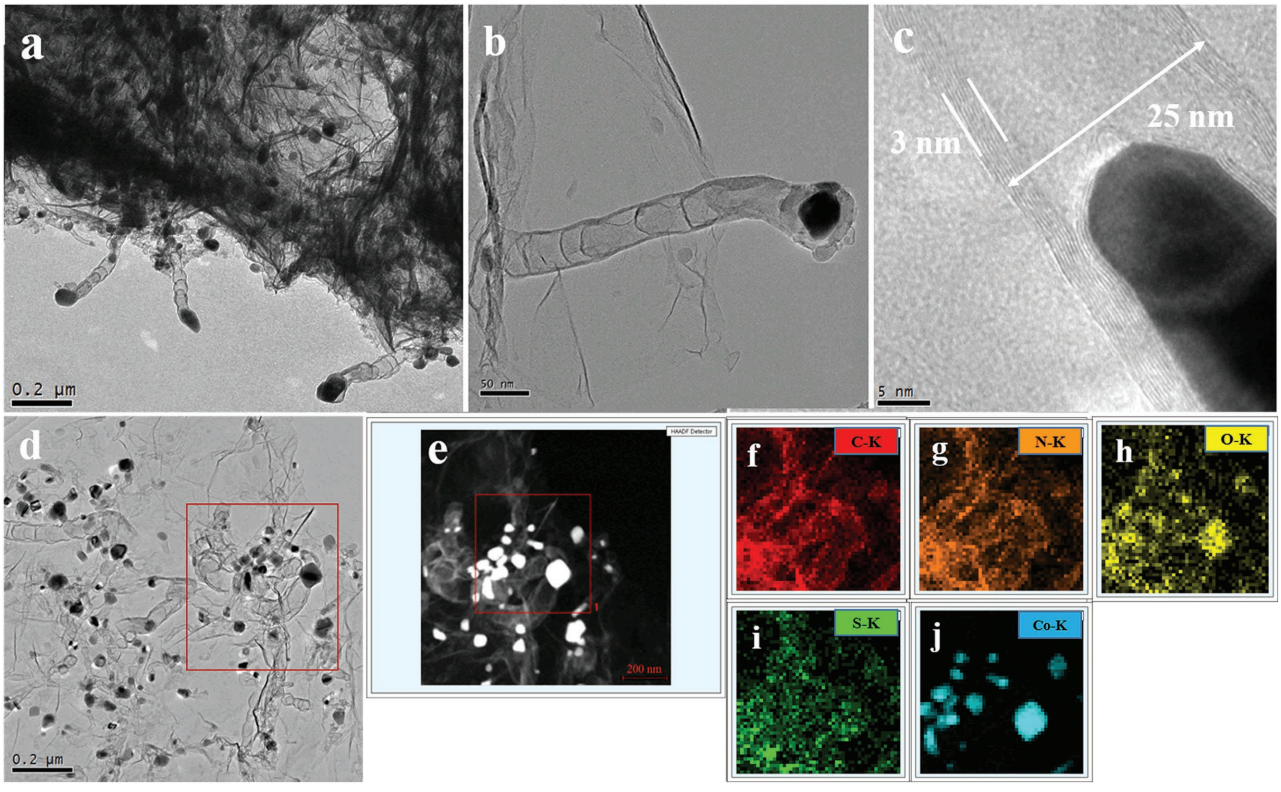

Figure 4. TEM images of a–c) GN–CNT matrix, d) S/GN–CNT composite. e) STEM image recorded by the high angle annular dark field detector, and EDS mapping of f) C, g) N, h) O, i) S, and j) Co of the selected region.

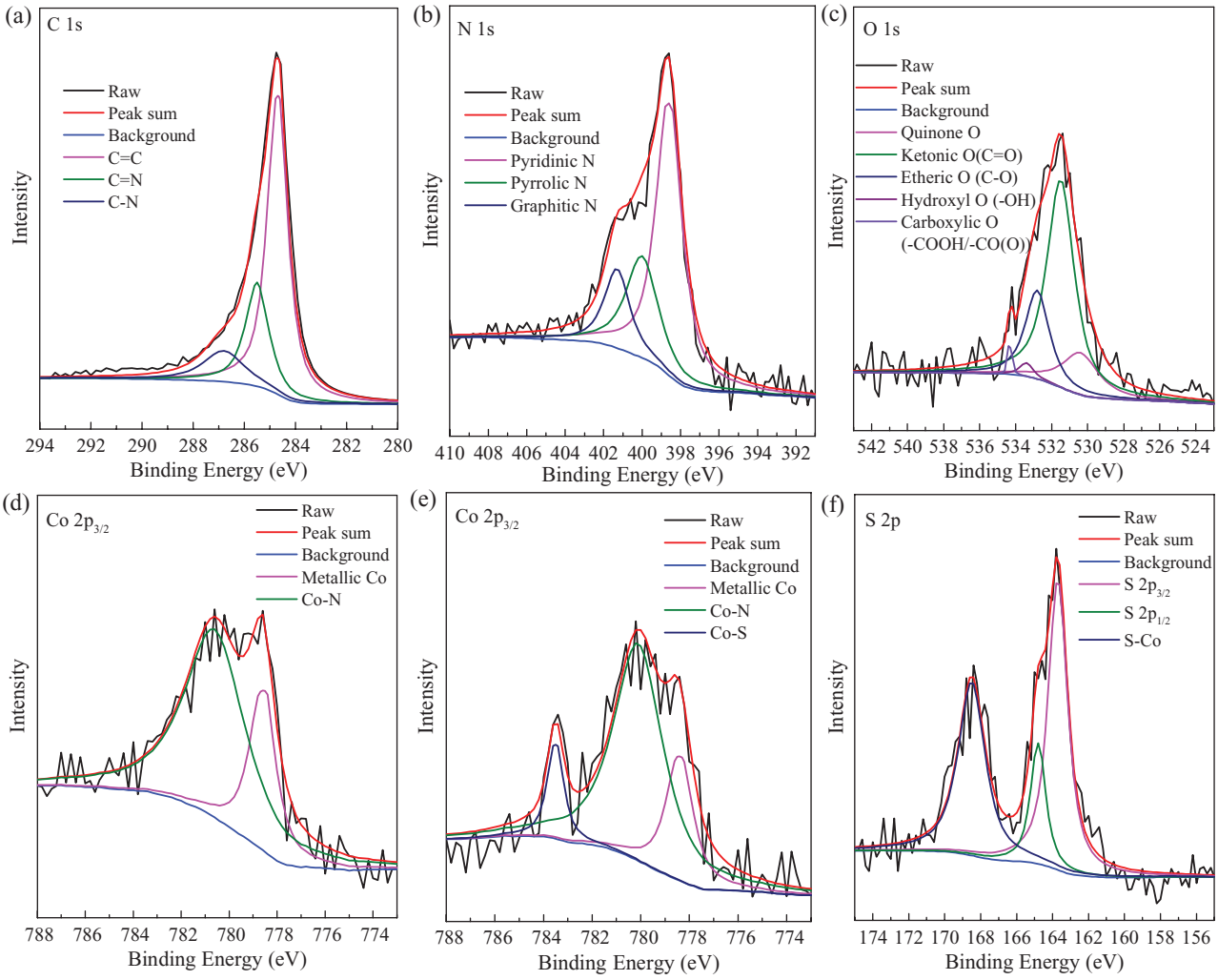

Figure 5. XPS spectra: a) C 1s, b) N 1s, c) O 1s, and d) Co $2p_{3/2}$ of the GN–CNT matrix. e) Co $2p_{3/2}$ and f) S 2p of the S/GN–CNT composite.

main pyridinic N chemical composition that offers two *p*-electrons, the GN–CNT matrix is believed to exhibit outstanding performance as a conductive Lewis base substrate for sulfur-based cathode.[20] Moreover, the Co $2p_{3/2}$ core level shows two characteristic peaks at 778.5 and 780.6 eV (Figure 5d), respectively. Typically, the binding energy at 778.5 eV is assigned to the metallic cobalt, while the higher binding energy at 780.6 eV is identified as the divalent cobalt (Co—N), possibly resulting by the incorporation of cobalt with the nitrogen species in the matrix.[21] Besides, the existence of O element is attributed to abundant oxygen-containing functional groups (Figure 5c), which are beneficial for confining sulfur species by chemical interaction. After introducing sulfur into the matrix, the metallic cobalt nanoparticles exhibit strong chemical interaction with sulfur species, as proved by the XPS spectra of S/GN–CNT composite. Apart from the typical peaks of the divalent cobalt (Co—N) and metallic cobalt, an extra peak at the higher binding energy of 783.5 eV is also observed (Figure 5e), which can be attributed to the higher oxidation state of cobalt. In the S 2p core level (Figure 5f), the peaks at 163.7 and 164.8 eV are assigned to S $2p_{3/2}$ and S $2p_{1/2}$, respectively, while the appearance of higher energy peak at 168.5 eV is attributed to the chemical bonding between cobalt and sulfur. Overall, the strong chemical bonding between cobalt nanoparticles and sulfur species can facilitate trapping and confining polysulfides in the discharge/charge processes, as well as the abundant doping elements of N and O. In addition, with the 3D connected structure, the GN–CNT matrix is believed to be a high-efficiency and stable substrate of sulfur for improving the performance of Li–S battery.

To get an insight into the electrochemical performance of the as-prepared S/C composites, typical cyclic voltammograms (CVs) at a scan rate of 0.1 mV s^{-1} with the potential range of 1.7–2.8 V are presented in **Figure 6**a. There are two cathodic peaks, associated with the formation of high-order PS_n ($4 \leq n \leq 8$) and insoluble Li_2S_2/Li_2S. Accordingly, in the subsequent anodic scan, two oxidation peaks are observed, corresponding to the oxidation of insoluble Li_2S_2/Li_2S to soluble polysulfides and polysulfides to sulfur element. While comparing with the contrast composites (Figure S5, Supporting Information), the S/GN–CNT composite possesses larger and stable current density of redox peaks in CVs, implying a low polarization, good

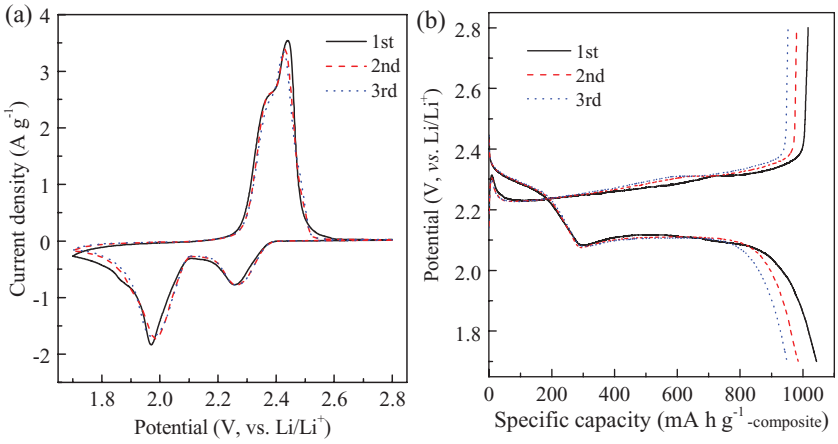

Figure 6. a) CV curves at the scan rate of 0.1 mV s^{-1} and b) initial three discharge/charge curves of S/GN–CNT composite at 0.1 C between 1.7 and 2.8 V.

reversibility, and promising cycle stability. Thus, the electrochemical performance of the S/C composites can be enhanced by introducing CNTs on the GN surface. The superiority in discharge capacity of S/GN–CNT composite can be proved obviously in the initial three discharge/charge curves (Figure 6b). The S/GN–CNT composite exhibits discharge capacities of 1049.6, 987.6, and 949.2 mA h g$^{-1}_{composite}$ in initial three cycles, much larger than that of the S/GN composite based on the composite as the cathode-active material (Figure S6, Supporting Information).

The cycle tests are carried out at various C rates to investigate the cycle stability and the rate capability of the S/GN–CNT composite. As shown in **Figure 7**a, the composite delivers a large discharge capacity of 1049.6 mA h g$^{-1}_{composite}$ in the initial cycle, and the capacity remains at 639.1 mA h g$^{-1}_{composite}$ even after 200 cycles. Actually, there is more information available when the S/C composite is used as active material, including the sulfur content in the composite, which is more valuable for the application of the composite in future battery system. Correspondingly, when calculated by the weight of sulfur, the initial discharge capacity is as high as 1373.8 mA h g$^{-1}_{sulfur}$, implying a high sulfur utilization of 82%, and the capacity remains at 836.5 mA h g$^{-1}_{sulfur}$ at 200th cycle. In contrast, the S/GN composite presents low discharge capacity and inferior capacity retention (Figure S7, Supporting Information). The enhancement in discharge capacity and cycle stability can be ascribed to effective intercalation and distribution of CNTs between graphene sheets with a strong covalent interaction, thus forming a unique 3D architectural structure for rapid electron transfer and favorable electrolyte infiltration. Besides, the presence of both cobalt nanoparticles and abundant heteroatoms (N, O) is also contributed to the improved performance owing to the strong chemical interaction with sulfur species. Particularly, although no CNTs but some particles are obtained in the matrix when urea is insufficient, the electrochemical performance of the corresponding S/C composite is still superior to that of S/GN. It can be easily understood by the contribution of the resultant porous structure, the produced Co nanoparticles, and doping elements created during the pyrolysis process of urea. On the contrary, GN suffers from the unavoidable restacking during the same heat treatment process, thus inducing a sharp decrease in SSA. Both the low SSA and poor conductivity undermine the electrochemical performance of the S/GN composite. On the other hand, it should be noted that the S/GN–CNT composite achieves the largest discharge capacity and the best cycle stability. It was reported that the presence of shorter CNTs on GN would make the matrix prone to exhibit higher capacitive behavior owing to the shorter Li^+ diffusion distance.[22] Thus, it is reasonable for the improved electrochemical performance for the S/C composite based on the GN–CNT matrix. While comparing with the S/A-MC11 hybrid composite in our previous work,[11d] the S/GN–CNT composite is still superior, owing to the advantage of graphene sheet in fabricating 3D structural matrix with CNTs than porous carbon spheres. Anyway, the sulfur-based composite, fabricated on the GN–CNT matrix, shows outstanding performance in discharge capacity and cycle stability at low C rate.

Moreover, the S/GN–CNT composite is expected to possess promising high rate capability owing to the unique 3D conductive structure. As indicated in Figure 7b, a large discharge capacity of 758.4 mA h g$^{-1}_{composite}$ is obtained at 0.5 C in the initial cycle, and remains at 463.7 mA h g$^{-1}_{composite}$ in the 500th cycle, indicating a low capacity decay

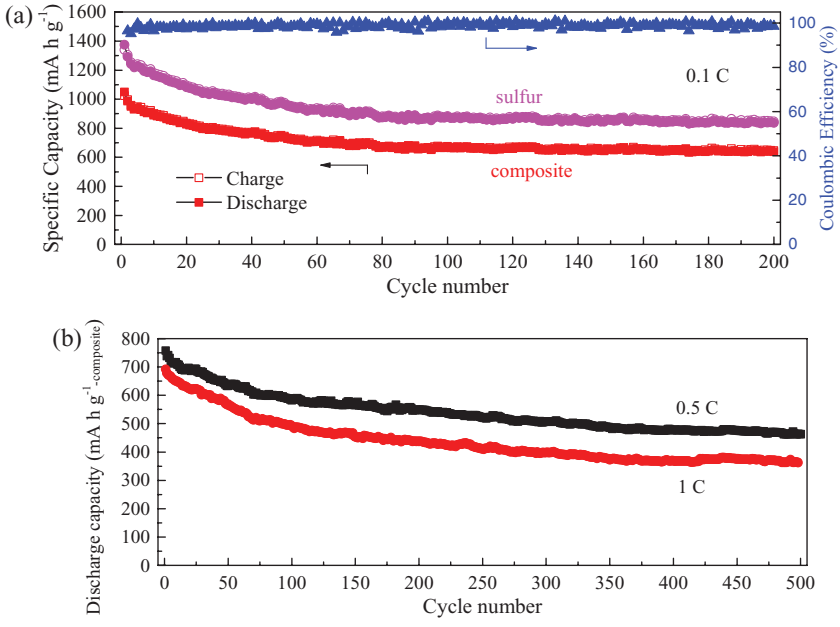

Figure 7. Long-term cycle tests of the S/GN–CNT composite at a) 0.1 C and b) 0.5 and 1 C.

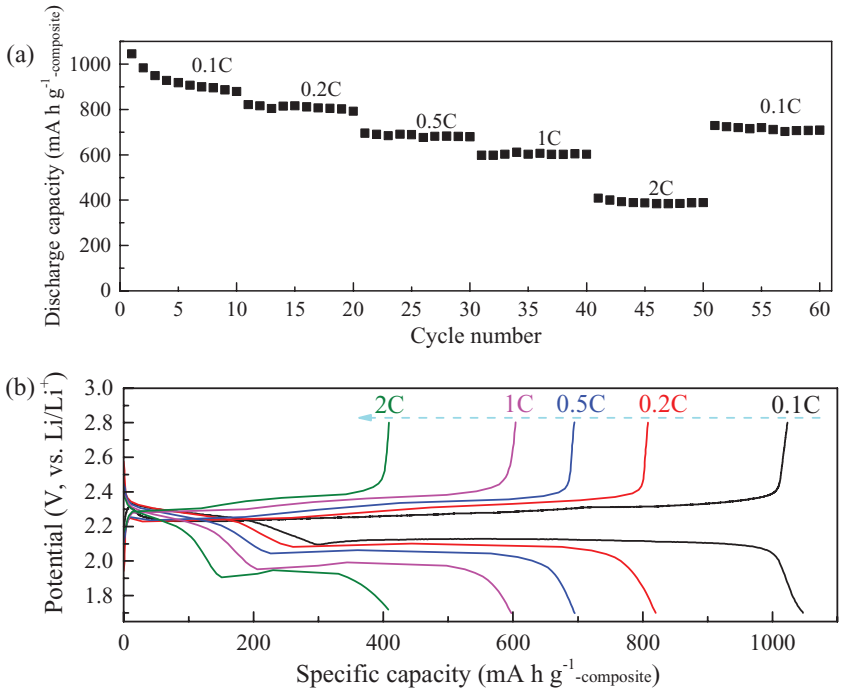

Figure 8. a) Rate capability and b) the initial discharge/charge curves of the S/GN–CNT composite at various C rates from 0.1 C to 2 C.

rate (CDR) of 0.08% per cycle. While the S/GN composite shows a rapid capacity decay from 598.0 mA h $g^{-1}_{composite}$ in the initial cycle to 186.9 mA h $g^{-1}_{composite}$ in the 300th cycle (CDR = 0.23% per cycle; Figure S7, Supporting Information). Furthermore, the S/GN–CNT composite delivers a discharge capacity of 363.5 mA h $g^{-1}_{composite}$ at 1 C in the 500th cycle with the CDR of 0.09% per cycle. On the other hand, as shown in **Figure 8**a, the S/GN–CNT composite offers the large discharge capacities of 1045.0, 821.1, 695.3, 598.0, and 408.6 mA h $g^{-1}_{composite}$ at various C rates from 0.1 to 2 C, which are more desirable than that of the S/GN composite (Figure S8a, Supporting Information). As to the discharge/charge curves, the shrinkage of both the high and low potential plateaus is observed in the two composites. However, the S/GN composite suffers more serious shrinkage simultaneously along with increasing the C rate. The low potential plateau disappears almost when the C rate is set at 1 C, which could be resulted from the poor conductivity and low diffusion of Li ions in the S/GN composite. Furthermore, the GN–CNT matrix is used to fabricate sulfur-based cathode with high sulfur loading (Figure S9, Supporting Information). The S/GN–CNT electrode (L_S = 2.5 mg cm^{-2}) exhibits a reversible discharge capacity of 478.8 mA h $g^{-1}_{composite}$ at 0.1 C in the 200th cycle, and the discharge capacity remains at 335.7 mA h $g^{-1}_{composite}$ when the sulfur loading is increased to 4.7 mg cm^{-2}. Both the two cells suffer a slow activation process within several initial cycles, owing to the progressive penetration of electrolyte in the thick sulfur cathode, but show good cycle stability with high sulfur loading. Overall, it is demonstrated from the satisfying electrochemical performance of S/GN–CNT composite that the 3D GN–CNT matrix is superior in incorporating with sulfur for fabricating high performance sulfur-based cathode. Here, the stable covalent linkage of CNTs and GN makes much more sense in improving the electrochemical performance of the S/GN–CNT composite. As shown in **Figure 9**, with the intercalation and distribution of CNTs between graphene layers, the GN–CNT matrix not only possesses relatively high specific surface area, but also presents an open and porous structure for good electron conduction, sufficient electrolyte penetration, and low diffusion impedance of Li ions. In addition, as shown in transmission electron microscopy (TEM) images, Co nanoparticles are wrapped in

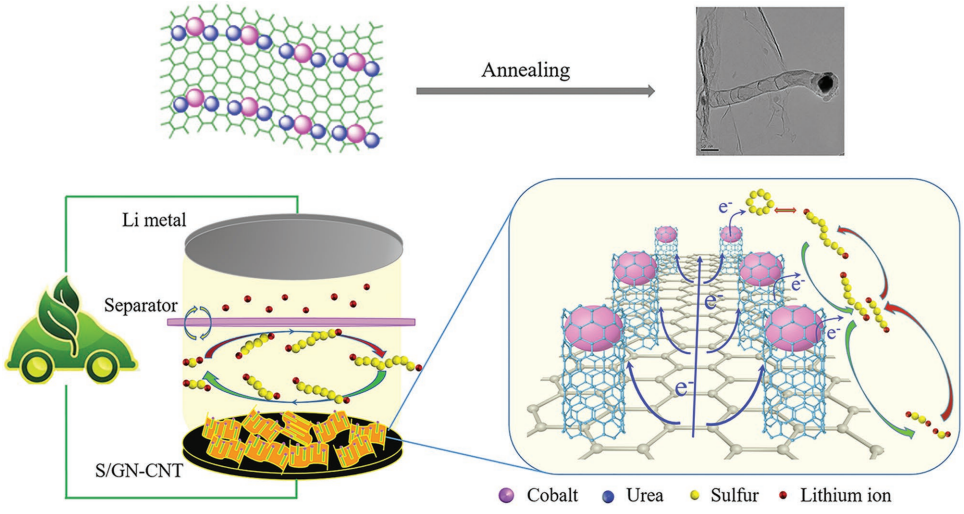

Figure 9. Schematic illustration of the preparation and structure for the GN–CNT matrix and the multipath rapid electron transfer for highly efficient redox reaction of the S/C composite.

the top of CNTs or distributed randomly among CNTs in the GN–CNT matrix and S/GN–CNT composite. The remaining metallic cobalt nanoparticles not only enhance the conductivity of sulfur cathodes, but show the strong chemical interaction with sulfur as indicated in the XPS analysis and elemental mapping. The metallic cobalt could be subsequently oxidized to form insoluble cobalt polysulfides or sulfides in the charge/discharge processes between 1.7 and 2.8 V (vs Li/Li^+).[23] It means that the strong immobilization of sulfur species by the existent cobalt could further suppress the polysulfide dissolution and facilitate the transformation between high-order and low-order polysulfides.[14d] The strategy involving metallic nanoparticles to enhance performance of sulfur cathodes is reported previously, such as copper nanoparticles[7e] and cobalt nanoparticles derived from cobalt-based organic framework materials.[14de] In the meantime, the GN–CNT matrix shows a good adsorption for polysulfides, which is measured by UV–vis adsorption spectra at 415 nm.[11g] As shown in **Figure 10**, GN shows the poor adsorption of polysulfides, while GN–CNT–H without Co nanoparticles presents the improved adsorption of polysulfides due to the porous structure and existence of heteroatoms (N, O). In particular, the strong adsorption of polysulfides can be obtained for the GN–CNT matrix, which is mainly attributed to the strong chemical interaction of polysulfides with Co and heteroatoms (N, O). All of these contributions make the S/GN–CNT composite showing outstanding electrochemical performance.

On the foundation of the analysis above, some essential measurements are employed to characterize the S/GN–CNT composite after 200 cycles. First, as clearly seen in XRD patterns (**Figure 11**), the cycled cathode shows typical peaks of orthorhombic sulfur and metallic cobalt, as compared with that of the blank C-coated Al foil. Noting the stronger peaks of orthorhombic sulfur than that of the S/A-MC11 composite in our previous work,[11d] it suggests better redox reversibility for S/GN–CNT cathode. TEM image of the cycled cathode material is given in **Figure 12**. Although carbon particles (Super P) cover completely the GN surface, and CNT with a diameter

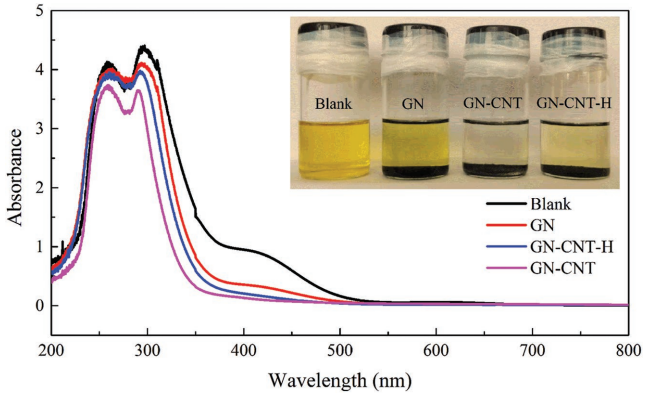

Figure 10. UV–vis adsorption spectra of Li_2S_6 solution. Inset: Digital photos of Li_2S_8 solution before and after contact with different absorbents. 0.01 M Li_2S_6 dissolved in DME/DOL (v/v, 1:1) and diluted to 0.002 M for the adsorption test. All the absorbents (10 mg) are dried in vacuum oven before adding into the Li_2S_6 solution. The sealed vials were kept in glove box overnight, and then the liquid supernatants were used for the UV–vis test.

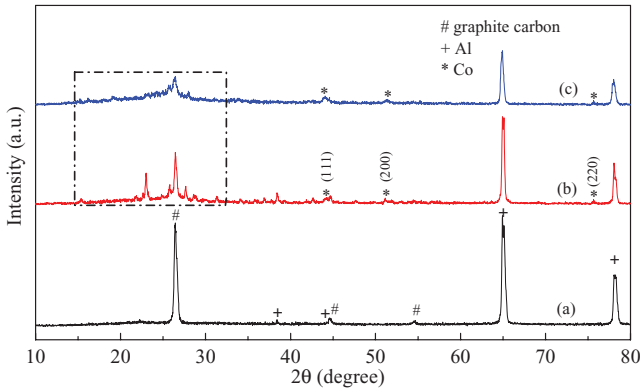

Figure 11. XRD patterns of a) C-coated Al foil and the S/GN-CNT electrodes b) before and c) after 200 cycles at 0.1 C.

of ≈70 nm is clearly observed adhering on the GN surface, implying the stable covalent interaction. Sulfur is still well-embedded in the GN–CNT matrix, as revealed by EDS mapping of the cathode material after 200 cycles. In addition, as seen in the Co mapping, much more teeny nanoparticles appear, suggesting regeneration during the long-term cycling. It seems that the chemical bonding between cobalt with sulfur species is broken and reformed repeatedly during the electrochemical reaction. Thus, the metallic cobalt not only serves as the catalyst for the growth of CNTs, but also helps to increase the specific capacity and rate capability by confining sulfur species with stable chemical interaction and facilitating the mutual transformation between high-order polysulfides and low-order ones. For the Li anodes shown in **Figure 13**, after long-term cycles, the surface cracks appear for both anodes in the cells based on S/GN and S/GN–CNT composites, compared with the fresh metallic Li (Figure S10, Supporting Information). In the cell with S/GN composite as cathode, the Li anode suffers severe damage, and large cracks are observed on the surface. Differently, in the cell with S/GN–CNT composite as cathode, Li anode shows a relatively smooth surface after 200 cycles. Meanwhile, the unavoidable deposition of insoluble Li_2S_2/Li_2S on the Li surface is weaker here, as shown in the S mapping on Li anode. It means that the GN–CNT matrix shows much more superior ability in capturing polysulfides than GN. Consequently, more polysulfides are mainly confined on the cathode side rather than travelling to the anode side, where the corrosion of metallic Li anode happens. Therefore, the rationally designed 3D GN–CNT matrix shows the desirable ability for capturing polysulfides, and subsequently protects the surface morphology of Li anode during the long-term cycles.

To get a further understanding with the contribution of the designed 3D structure on the performance, electrochemical impedance spectra (EIS) are measured as shown in **Figure 14**a. At full charged state, two depressed semicircles in the high-frequency (HF) region and a sloped line in the low-frequency (LF) region can be observed in all the impedance plots. Specifically, the former semicircle in the HF region is considered as the contribution of the resistance (R_L) and capacitance (CPE1) on electrolyte and electrode interface resulting from the deposition of the insoluble Li_2S_2/Li_2S layer within the discharge/charge cycles. The latter semicircle is mainly consisted of the

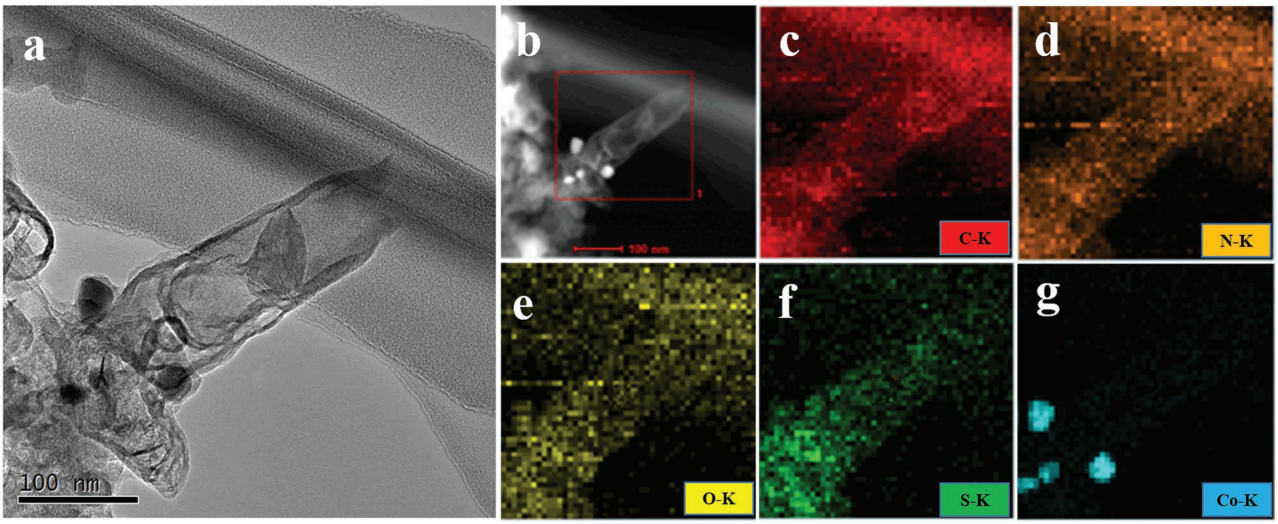

Figure 12. a) TEM image of S/GN–CNT composite after 200 cycles at 0.1 C. b) STEM image and EDS mapping of c) C, d) N, e) O, f) S, and g) Co elements in the selected region.

charge-transfer resistance (R_{ct}) and relative capacitance (CPE2). The sloped line in the LF region is ascribed to the semi-infinite Warburg diffusion process of Li ions in the electrode.[24,25] The impedance plots before discharge are consisted of a depressed semicircle and a sloped line, and the equivalent circuit used to fit the values of the involved resistance at full charged state is presented in Figure S11 (Supporting Information), and the simulated values are given in Table S1 (Supporting Information). Taking a visual focus on Figure 14b, the electrolyte resistances (R_s) in both cells are quite close, and increase slightly along with subsequent cycling, resulting from the higher viscosity and lower Li^+ mobility caused by the dissolution of polysulfides in the electrolyte. In the cell with S/GN–CNT composite, R_{ct} decreases rapidly from 31.2 Ω before discharge to the lowest value (5.8 Ω) in the 5th cycle, revealing the surface electrochemical activity is initiated along with the charge/discharge processes. In the following cycles, it increases gradually to 9.6 Ω in the 200th cycle. The extremely low value of R_{ct} implicates

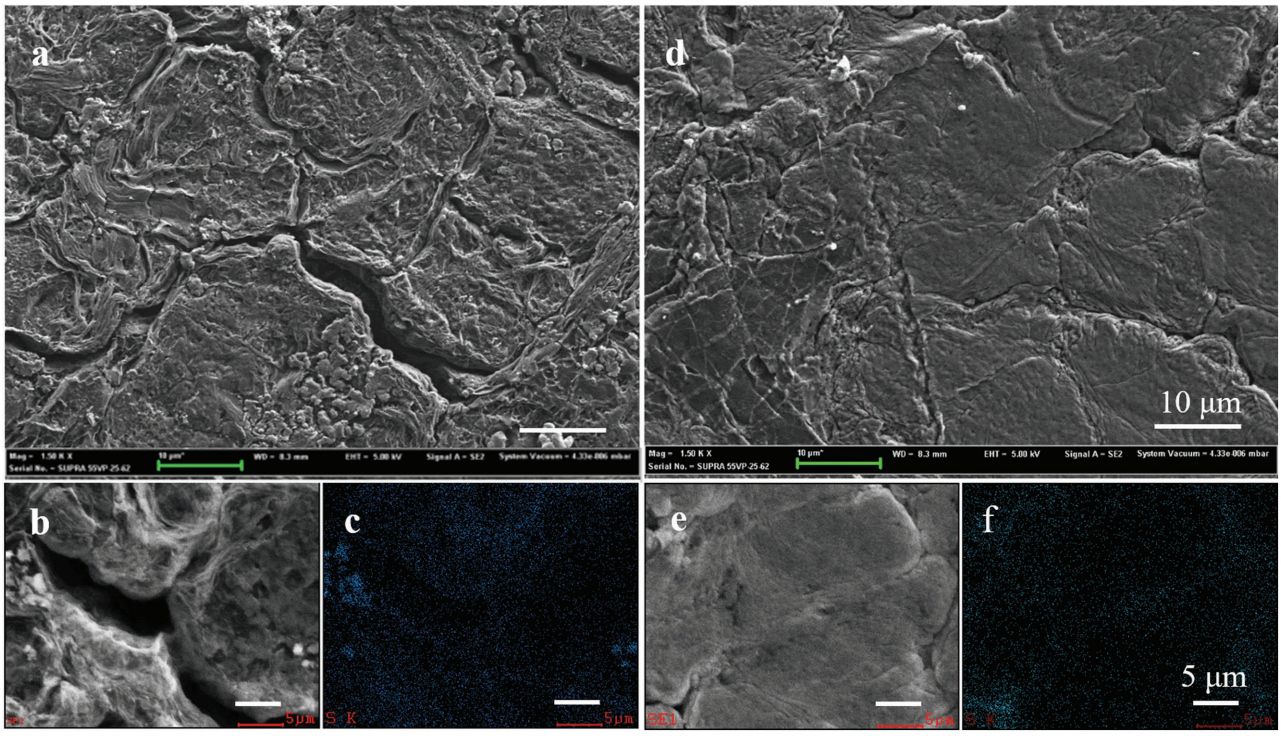

Figure 13. SEM images and the map of elemental S of Li anodes after 200 cycles in the cells based on a–c) S/GN composite and d–f) S/GN–CNT composite. The Li anodes are taken out from the cells and soaked in DME for a while to dissolve the remaining Li salt (LiTFSI).

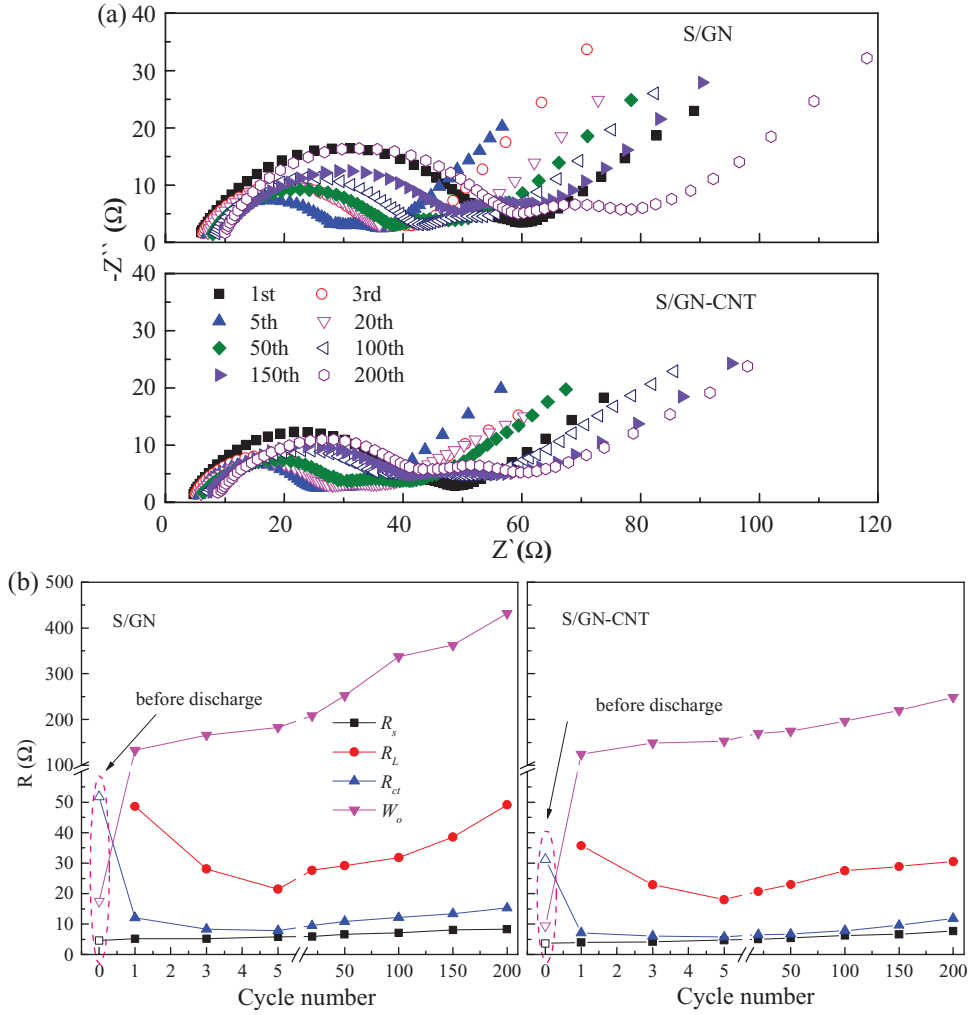

Figure 14. a) EIS after fully charged to 2.8 V at 0.1 C for different cycles and b) the fitted data of the as-prepared S/GN and S/GN–CNT composites. (R_s: the resistance of the electrolyte; R_L: the resistance of the insoluble Li_2S_2/Li_2S layer; R_{ct}: the charge-transfer resistance; W_o: the semi-infinite Warburg diffusion impedance.)

the superior electrochemical activity due to the highly 3D conductive structure of the GN–CNT matrix, thus leading to a high utilization of active sulfur. The same variation tendency can be found with R_L. A slight decrease of R_L within the initial five cycles is observed owing to the relocation of sulfur active materials in the cathode, which might reduce the tendency of forming the passivation layer.[26] Then, it slightly increases in the following cycles since the gradual increase in the thickness of Li_2S_2/Li_2S layer. As seen in the diffusion process, the Warburg impedance (W_o) increases from 124.1 Ω in the 1st cycle to 248.4 Ω in the 200th cycle, which is nearly 30-fold larger than that in before-discharge state (9.4 Ω). It is believed that the irreversible deposition and aggregation of Li_2S_2/Li_2S layer on the surface of the cathode become more serious during cycling.

Notably, the EIS data reveal a much lower value of R_L, R_{ct}, and W_o of the S/GN–CNT composite than that of the S/GN composite. The intercalation and distribution of CNTs between graphene sheets promote the surface charge-transfer and ion diffusion in the electrode by providing abundant pathways and shorter diffusion distances. Such a unique 3D structural GN–CNT matrix with dispersion of cobalt nanoparticles and abundant doping elements, in which CNTs are covalently anchored on graphene nanosheet, enables rapid electronic and ionic transport, and increases the electrochemical kinetics of the corresponding S/C composite, resulting in the superiority of discharge capacity, high rate capability, and cycle stability.

As the desired sulfur cathode, the good electronic conductivity is indispensable for charge transfer in the electrochemical redox reaction of sulfur active material. Meanwhile, the porous electrode structure should be fabricated in order to provide good mass transfer between electrolyte and electrode interface for realizing such redox reaction. Here, the GN–CNT matrix shows the excellent electronic conductivity due to the formation of 3D interpenetrating conductive network. The electrolyte can readily reach the interface of the porous electrode through 3D interpenetrating structure of the GN–CNT matrix. Therefore, the high utilization of sulfur active material, large discharge capacity, and good rate capability of the S/GN–CNT composite can be obtained. Moreover, the coexistence of Co nanoparticles and heteroatoms (N, O) in the as-prepared 3D GN–CNT matrix

is highly significant to immobilize sulfur species and suppress polysulfide dissolution by the strong adsorption and chemical interaction, resulting in the good cycle stability of the S/GN–CNT composite.

3. Conclusion

In summary, 3D architectural GN–CNT matrix can be obtained via the pyrolysis of urea on GN surface with the presence of Co^{2+}, and the length and density of the grown CNTs can be easily tuned by changing the amount of additive urea. Finally, the as-prepared S/GN–CNT composite based on the GN–CNT matrix exhibits high initial discharge capacity and slow capacity decay of 0.08% and 0.09% per cycle, respectively, at 0.5 and 1.0 C within 500 cycles. It is believed that the enhanced electrochemical performance can be ascribed to three reasons: (1) the rational designed 3D GN–CNT matrix with open and porous structure offers more pathways for rapid transfer of electron and accelerates electrolyte penetration; (2) the presence of strong chemical interaction between cobalt nanoparticles and sulfur species is beneficial for trapping and confining polysulfides, and facilitating the mutual transformation between high-order polysulfides and low-order ones; (3) the doping element N makes the matrix serve as a conductive Lewis base substrate, which shows strong interaction with polysulfides.

4. Experimental Section

Preparation and Characterization: To obtain the GN–CNT matrix, GO was first prepared by oxidizing graphite power via an improved method.[27] GO (0.2 g) was dispersed in pure water for 1 h in an ultrasonic bath to obtain GO suspension (1 mg mL^{-1}). Then, 1 mmol cobalt(II) nitrate hexahydrate (analytical grade) was added into the solution, followed by stirring for 4 h at room temperature. After that, urea (6.0 g) was added into the above solution, and then stirred continuously at 80 °C to obtain dried powder. Finally, the powder was calcined at 900 °C for 1 h under argon atmosphere to obtain GN–CNT matrix. The S/GN–CNT composite was fabricated via chemical deposition method. In a typical procedure, 0.02 mol $Na_2S_2O_3{\cdot}5H_2O$ (analytical grade) was first dissolved in deionized water (200 mL) containing 1 wt% of polyvinylpyrrolidone (PVP, k30). Then, GN–CNT matrix (0.16 g) was added and the mixture underwent an ultrasonic treatment to obtain a homogeneous suspension. Finally, a certain amount of hydrochloric acid solution (5 wt%) was added drop by drop, followed by vigorously stirring for about 2 h for complete precipitation of sulfur. The reaction can be expressed as $S_2O_3^{2-} + 2H^+ \rightarrow S\downarrow + SO_2\uparrow + H_2O$. The composites were centrifuged and washed repeatedly with deionized water and ethanol, and dried in a vacuum oven at 50 °C for 24 h. As the contrast samples, GN–CNT-*x* (*x* = 3, 9, 15) matrices were also prepared in the same procedure with the different amount of additive urea, as well as GN, which was prepared by directly annealing GO without adding anything else. Then, all the contrast S/C composites were prepared in the same way. The as-prepared products were characterized by X-ray diffraction (Rigaku mini FlexII) with the 2θ range from 10° to 80°. The sulfur content in the obtained composites was confirmed by thermogravimetric analyzer (METTLER TOLEDO, TGA/DSC1) under argon atmosphere. The Brunauer–Emmett–Teller measurement using N_2 absorption was performed on JW-BK112 system. Raman spectroscopy was performed on a DXR Microscope system with a 633 nm laser. Li_2S_6 solutions before and after contact with various absorbents were tested by UV–visible absorption spectrophotometry (UV–vis, Varian Cary 100 Conc). Surface chemistry was analyzed by XPS in PHI-5000 Versa-Probe with Mg Kα radiation of 1253.6 eV. The microstructure and morphology of the composites were identified by SEM (Supra 55VP) and TEM (FEI, Tecnai F20).

Electrochemical Measurement: To prepare the working electrode, a slurry was obtained by mixing and stirring the as-prepared S/C composites, Super P and polyvinyldifluoride (PVDF) with the mass ratio of 7:2:1 in *N*-methyl-2-pyrrolidone, respectively. Then, the slurry was coated onto the C-coated Al foil and dried in vacuum oven at 50 °C for 12 h. Finally, the film was punched into disks with a diameter of 12 mm. The sulfur loading (L_S) of each composite was controlled at 1.3–1.6 mg cm^{-2}. Coin-type cells (2032) were assembled with metallic Li as the counter and reference electrodes and Celgard 2300 as a separator. The electrolyte was consisted of 1.0 M lithium bis(trifluoromethanesulfonyl)imide (LiTFSI) in 1,3-dioxolane (DOL) and 1,2-dimethoxyethane (DME) (v/v, 1:1) with 0.2 M $LiNO_3$ as the additive. The volume of the electrolyte used in each cell was 30–50 µL, and the electrolyte-to-sulfur (E/S) ratio was about 15–20 µL mg^{-1}. Discharge/charge tests were carried out between 1.7 and 2.8 V (vs Li/Li^+) at various C rates (1 C = 1675 mA h g^{-1}) with LAND-CT2001A instruments (Wuhan Jinnuo, China). The specific capacities were calculated based on the S/C composite as the cathode-active material. CV measurements were performed on electrochemical workstation (CHI 600A, Shanghai Chenhua) with a scan rate of 0.1 mV s^{-1}. In addition, EIS were performed using electrochemical workstation (Zahner IM6ex) in the frequency range of 10 mHz to 100 kHz, while the disturbance amplitude was set at 5 mV.

Supporting Information

Supporting Information is available from the Wiley Online Library or from the author.

Acknowledgements

Financial support from the New Energy Project for Electric Vehicles in National Key Research and Development Program (2016YFB0100200), NFSC (21573114, 51502145, and 21421001) of China is gratefully acknowledged.

Received: November 16, 2016
Revised: December 9, 2016
Published online: January 27, 2017

[1] a) M. K. Song, E. J. Cairns, Y. G. Zhang, *Nanoscale* **2013**, *5*, 2186; b) M. Barghamadi, A. S. Best, A. I. Bhatt, A. F. Hollenkamp, M. Musameh, R. J. Rees, T. Rüther, *Energy Environ. Sci.* **2014**, *7*, 3902.
[2] a) X. P. Gao, H. X. Yang, *Energy Environ. Sci.* **2010**, *3*, 174; b) G. L. Xu, Q. Wang, J. C. Fang, Y. F. Xu, J. T. Li, L. Huang, S. G. Sun, *J. Mater. Chem. A* **2014**, *2*, 19941; c) X. Fang, H. S. Peng, *Small* **2015**, *11*, 1488.
[3] a) A. Manthiram, Y. Z. Fu, S. H. Chung, C. X. Zu, Y. S. Su, *Chem. Rev.* **2014**, *114*, 11751; b) Z. Li, Y. M. Huang, L. X. Yuan, Z. X. Hao, Y. H. Huang, *Carbon* **2015**, *92*, 41.
[4] a) Y. V. Mikhaylik, J. R. Akridge, *J. Electrochem. Soc.* **2004**, *151*, A1969; b) S. S. Zhang, *J. Power Sources* **2013**, *231*, 153; c) G. Y. Xu, B. Ding, J. Pan, P. Nie, L. F. Shen, X. G. Zhang, *J. Mater. Chem. A* **2014**, *2*, 12662; d) R. J. Chen, T. Zhao, F. Wu, *J. Power Sources* **2013**, *231*, 153.
[5] A. Manthiram, S. H. Chung, C. X. Zu, *Adv. Mater.* **2015**, *27*, 1980.
[6] a) Y. Yang, G. Y. Zheng, Y. Cui, *Chem. Soc. Rev.* **2013**, *42*, 3018; b) J. Gao, H. D. Abruña, *J. Phys. Chem. Lett.* **2014**, *5*, 882.
[7] a) B. Zhang, X. Qin, G. R. Li, X. P. Gao, *Energy Environ. Sci.* **2010**, *3*, 1531; b) J. Schuster, G. He, B. Mandlmeire, T. Yim, K. T. Lee,

T. Bein, L. F. Nazar, *Angew. Chem., Int. Ed.* **2012**, *51*, 3591; c) H. Ye, Y. X. Yin, S. Xin, Y. G. Guo, *J. Mater. Chem. A* **2013**, *1*, 6602; d) X. F. Yang, N. Yan, W. Zhou, H. Z. Zhang, X. F. Li, H. M. Zhang, *J. Mater. Chem. A* **2015**, *3*, 15314; e) S. Y. Zheng, F. Yi, Z. P. Li, Y. J. Zhu, Y. H. Xu, C. Luo, J. H. Yang, C. S. Wang, *Adv. Funct. Mater.* **2014**, *24*, 4156.

[8] a) N. Jayaprakash, J. Shen, S. S. Moganty, A. Corona, L. A. Archer, *Angew. Chem., Int. Ed.* **2011**, *50*, 5904; b) C. F. Zhang, H. B. Wu, C. Z. Yuan, Z. P. Guo, X. W. Lou, *Angew. Chem., Int. Ed.* **2012**, *51*, 9592; c) W. D. Zhou, X. C. Xiao, M. Cai, L. Yang, *Nano Lett.* **2014**, *14*, 5250; d) W. D. Zhou, C. M. Wang, Q. L. Zhang, H. D. Abruña, Y. He, J. W. Wang, S. X. Mao, X. C. Xiao, *Adv. Energy Mater.* **2015**, *5*, 1401752.

[9] a) Y. S. Su, Y. Z. Fu, A. Manthiram, *Phys. Chem. Chem. Phys.* **2012**, *14*, 14495; b) J. J. Chen, Q. Zhang, Y. N. Shi, L. L. Qin, Y. Cao, M. S. Zheng, Q. F. Dong, *Phys. Chem. Chem. Phys.* **2012**, *14*, 5376; c) C. H. Wang, H. W. Chen, W. L. Dong, J. Ge, W. Lu, X. D. Wu, L. Guo, L. W. Chen, *Chem. Commun.* **2014**, *50*, 1202; d) L. Sun, M. Y. Li, Y. Jiang, W. B. Kong, K. L. Jiang, J. P. Wang, S. S. Fan, *Nano Lett.* **2014**, *14*, 4044; e) X. Pu, G. Yang, C. Yu, *Adv. Mater.* **2014**, *26*, 7456; f) K. Xi, B. A. Chen, H. L. Li, R. S. Xie, C. L. Gao, C. Zhang, R. V. Kumar, J. Robertson, *Nano Energy* **2015**, *12*, 538; g) K. Fu, Y. P. Li, M. Dirican, C. Chen, Y. Lu, J. D. Zhu, Y. Li, L. Y. Cao, P. D. Bradford, X. W. Zhang, *Chem. Commun.* **2014**, *50*, 10277; h) H. S. Kang, Y. K. Sun, *Adv. Funct. Mater.* **2016**, *26*, 1225.

[10] a) H. Kim, H. D. Lim, J. S. Kim, K. Kang, *J. Mater. Chem. A* **2014**, *2*, 33; b) J. P. Rong, M. Y. Ge, X. Fang, C. W. Zhou, *Nano Lett.* **2014**, *14*, 473; c) X. F. Gao, J. Y. Li, D. S. Guan, C. Yuan, *ACS Appl. Mater. Interfaces* **2014**, *6*, 4154; d) C. Zhang, D. H. Liu, W. Lv, D. W. Wang, W. Wei, G. M. Zhou, S. G. Wang, F. Li, B. H. Li, F. Y. Kang, Q. H. Yang, *Nanoscale* **2015**, *7*, 5592; e) S. Y. Yuan, Z. Y. Guo, L. N. Wang, S. Hu, Y. G. Wang, Y. Y. Xia, *Adv. Sci.* **2015**, *2*, 1500071; f) R. P. Fang, S. Y. Zhao, S. F. Pei, X. T. Qian, P. X. Hou, H. M. Cheng, C. Liu, F. Li, *ACS Nano* **2016**, *10*, 8676; g) S. T. Lu, Y. Chen, X. H. Wu, Z. D. Yang, Y. Li, *Sci. Rep.* **2014**, *4*, 4629; h) Y. Chen, S. T. Lu, J. Zhou, X. H. Wu, W. Qin, O. Ogoke, G. Wu, *J. Mater. Chem. A* **2016**, DOI: 10.1039/c6ta08039a.

[11] a) J. Xie, J. Yang, X. Y. Zhou, Y. L. Zou, J. J. Tang, S. C. Wang, F. Chen, *J. Power Sources* **2014**, *253*, 55; b) Y. M. Chen, X. Y. Li, K. S. Park, J. H. Hong, J. Song, L. M. Zhou, Y. W. Mai, H. T. Huang, J. B. Goodenough, *J. Mater. Chem. A* **2014**, *2*, 10126; c) J. X. Song, M. L. Gordin, T. Xu, S. R. Chen, Z. X. Yu, H. Sohm, J. Lu, Y. Ren, Y. H. Duan, D. H. Wang, *Angew. Chem.* **2015**, *127*, 4399; d) Z. Zhang, H. K. Jing, S. Liu, G. R. Li, X. P. Gao, *J. Mater. Chem. A* **2015**, *3*, 6827; e) G. J. Hu, C. Xu, Z. H. Sun, S. G. Wang, H. M. Cheng, F. Li, W. C. Ren, *Adv. Mater.* **2016**, *28*, 1603; f) S. T. Lu, Y. W. Cheng, X. H. W. J. Liu, *Nano Lett.* **2013**, *13*, 2485; g) J. X. Song, M. L. Gordin, T. Xu, S. R. Chen, Z. X. Yu, H. Sohn, J. Lu, Y. Ren, Y. H. Duan, D. H. Wang, *Angew. Chem., Int. Ed.* **2015**, *54*, 4325.

[12] a) G. C. Li, G. R. Li, S. H. Ye, X. P. Gao, *Adv. Energy Mater.* **2012**, *2*, 1238; b) W. D. Zhou, Y. C. Yu, H. Chen, F. J. DiSalvo, H. D. Abruña, *J. Am. Chem. Soc.* **2013**, *135*, 16736; c) W. Y. Li, Q. F. Zhang, G. Y. Zheng, Z. W. Seh, H. B. Yao, Y. Cui, *Nano Lett.* **2013**, *13*, 5534; d) G. Q. Ma, Z. Y. Wen, J. Jin, Y. Lu, X. W. Wu, M. F. Wu, C. H. Chen, *J. Mater. Chem. A* **2014**, *2*, 10350; e) H. Cheng, S. P. Wang, *J. Mater. Chem. A* **2014**, *2*, 13783.

[13] a) Z. W. Seh, W. Li, J. J. Cha, G. Zheng, Y. Yang, M. T. McDowell, P. C. Hsu, Y. Cui, *Nat. Commun.* **2013**, *4*, 1331; b) X. Liang, C. Hart, Q. Pang, A. Garsuch, T. Weiss, L. F. Nazar, *Nat. Commun.* **2015**, *6*, 4759; c) C. J. Hart, M. Cuisinier, X. Liang, D. Kundu, A. Garsuch, L. F. Nazar, *Chem. Commun.* **2015**, *51*, 2308; d) X. Y. Tao, J. G. Wang, C. Liu, H. T. Wang, H. B. Yao, G. Y. Zheng, Z. W. Seh, Q. X. Cai, W. Y. Li, G. M. Zhou, C. X. Zu, Y. Cui, *Nat. Commun.* **2016**, *7*, 11203; e) X. Liang, C. Y. Kwok, F. Lodi-Marzano, Q. Pang, M. Cuisinier, H. Huang, C. J. Hart, D. Houtarde, K. Kaup, H. Sommer, T. Brezesinski, J. Janek, L. F. Nazar, *Adv. Energy Mater.* **2016**, *6*, 1501636.

[14] a) G. Y. Xu, B. D, L. F. Shen, P. Nie, J. P. Han, X. G. Zhang, *J. Mater. Chem. A* **2013**, *1*, 4490; b) J. W. Zhou, R. Li, X. X. Fan, Y. F. Chen, R. D. Han, W. Li, J. Zheng, B. Wang, X. G. Li, *Energy Environ. Sci.* **2014**, *7*, 2715; c) Z. Q. Wang, B. X. Wang, Y. Yang, Y. J. Cui, Z. Y. Wang, B. L. Chen, G. D. Qian, *ACS Appl. Mater. Interfaces* **2015**, *7*, 20999; d) Y. J. Li, J. M. Fan, M. S. Zheng, Q. F. Dong, *Energy Environ. Sci.* **2016**, *9*, 1998; e) Z. Q. Li, C. X. Li, X. L. Ge, J. Y. Ma, Z. W. Zhang, Q. Li, C. X. Wang, L. W. Yin, *Nano Energy* **2016**, *23*, 15; f) Z. A. Ghazi, L. Y. Zhu, H. Wang, A. Naeem, A. M. Khattak, B. Liang, N. A. Khan, Z. X. Wei, L. S. Li, Z. Y. Tang, *Adv. Energy Mater.* **2016**,*6*, 1601250; g) H. P. Liao, H. M. Wang, H. M. Ding, X. S. Meng, H. Xu, B. S. Wang, X. P. Ai, C. Wang, *J. Mater. Chem. A* **2016**, *4*, 7416.

[15] a) R. J. Chen, T. Zhao, J. Lu, F. Wu, L. Li, J. Z. Chen, G. Q. Tan, Y. S. Ye, K. Amine, *Nano Lett.* **2013**, *13*, 4642; b) J. Xie, J. Yang, X. Y. Zhou, Y. L. Zou, J. J. Tang, S. C. Wang, F. Chen, *J. Power Sources* **2014**, *253*, 55; c) L. Sun, W. B. Kong, Y. Jiang, H. C. Wu, K. L. Jiang, J. P. Wang, S. S. Fan, *J. Mater. Chem. A* **2015**, *3*, 5305; d) Y. Chen, S. T. Lu, X. H. Wu, J. Liu, *J. Phys. Chem. C* **2015**, *119*, 10288.

[16] a) M. Q. Zhao, X. F. Liu, Q. Zhang, G. L. Tian, J. Q. Huang, W. C. Zhu, F. Wei, *ACS Nano* **2012**, *6*, 10759; b) H. J. Peng, J. Q. Huang, M. Q. Zhao, Q. Zhang, X. B. Cheng, X. Y. Liu, W. Z. Qian, F. Wei, *Adv. Funct. Mater.* **2014**, *24*, 2772; c) C. Tang, Q. Zhang, M. Q. Zhao, J. Q. Huang, X. B. Cheng, G. L. Tian, H. J. Peng, F. Wei, *Adv. Mater.* **2014**, *26*, 6100.

[17] Z. Y. Yang, Y. F. Zhao, Q. Q. Xiao, Y. X. Zhang, L. Jing, Y. M. Yan, K. N. Sun, *ACS Appl. Mater. Interfaces* **2014**, *6*, 8497.

[18] Z. Lin, G. Waller, Y. Liu, M. Liu, C. P. Wong, *Adv. Energy Mater.* **2012**, *2*, 884.

[19] a) C. H. See, A. T. Harris, *Ind. Eng. Chem. Res.* **2007**, *46*, 997; b) K. Otsuka, Y. Abe, N. Kanai, Y. Kobayashi, S. Takenaka, E. Tanabe, *Carbon* **2004**, *42*, 727; c) X. P. Gao, Y. Zhang, X. Chen, G. L. Pan, J. Yan, F. Wu, H. T. Yuan, D. Y. Song, *Carbon* **2004**, *42*, 47.

[20] J. J. Chen, R. M. Yuan, J. M. Feng, Q. Zhang, J. X. Huang, G. Fu, M. S. Zheng, B. Ren, Q. F. Dong, *Chem. Mater.* **2015**, *27*, 2048.

[21] Z. Xiang, Y. Xue, D. Cao, L. Huang, J. F. Chen, L. Dai, *Angew. Chem., Int. Ed.* **2014**, *53*, 2433.

[22] L. Basirico, G. Lanzara, *Nanotechnology* **2012**, *23*, 305401.

[23] a) A. Debart, L. Dupont, R. Patrice, J. M. Tarascon, *Solid State Sci.* **2006**, *8*, 640; b) Y. Kim, J. B. Goodenough, *J. Phys. Chem. C* **2008**, *112*, 15060.

[24] Z. F. Deng, Z. A. Zhang, Y. Q. Lai, J. Liu, J. Li, Y. X. Liu, *J. Electrochem. Soc.* **2013**, *160*, A553.

[25] V. S. Kolosnitsyn, E. V. Kuzmina, E. V. Karaseva, S. E. Mochalov, *J. Power Sources* **2011**, *196*, 1478.

[26] C. X. Zu, Y. S. Su, Y. Z. Fu, A. Manthiram, *Phys. Chem. Chem. Phys.* **2013**, *15*, 2291.

[27] D. C. Marcano, D. V. Kosynkin, J. M. Berlin, A. Sinitskii, Z. Z. Sun, A. Slesarev, L. B. Alemany, W. Lu, J. M. Tour, *ACS Nano* **2010**, *4*, 4806.